DEPENDENCY OF SEA DRAG ON THE WAVE SLOPE

Wagih Abu Rowin
Department of Mechanical Engineering
University of Melbourne
Parkville, Victoria 3010, Australia
waburowin@unimelb.edu.au

Kevin
Department of Mechanical Engineering
University of Melbourne
Parkville, Victoria 3010, Australia
kevin.kevin@unimelb.edu.au

Tunggul Bhirawa
Marine Biophysics Unit
Okinawa Institute of Science and Technology
Onna-son, 904-0495, Okinawa, Japan
tunggul.bhirawa@oist.jp

Junghoon Lee
Platforms division
Defence Science and Technology group
Melbourne, Victoria 3207, Australia
junghoon.lee@defence.gov.au

Jimmy Philip
Department of Mechanical Engineering
University of Melbourne
Parkville, Victoria 3010, Australia
jimmyp@unimelb.edu.au

Ivan Marusic
Department of Mechanical Engineering
University of Melbourne
Parkville, Victoria 3010, Australia
imarusic@unimelb.edu.au

Jason Monty
Department of Mechanical Engineering
University of Melbourne
Parkville, Victoria 3010, Australia
montyjp@unimelb.edu.au

ABSTRACT

The dynamic interplay between the ocean and the atmosphere is pivotal in shaping various environmental parameters such as heat flux, momentum exchanges and aerosol dispersion. An in-depth understanding of this complex interaction, particularly the dynamics between ocean waves and turbulent airflow at the air-water interface, remains a focal point of ongoing research efforts. In this experimental investigation, we delve into the turbulence levels occurring over wind waves, with a specific focus on the impact of wave slope on turbulence dynamics. Employing Particle Image Velocimetry (PIV) experiments with high magnification, we detect turbulent flow separation events occurring near wave crest regions. Our analysis reveals a pronounced influence of wave slope on Reynolds stress below the wave crest, notably with the contribution from flow over the leeward faces of the wave on Reynolds stress surpassing that of the windward face by approximately twofold. Interestingly, above the wave crest, contributions from both sides of the wave exhibit some similarities, despite the wave induced motions extending to approximately the edge of the boundary layer.

INTRODUCTION

The intricate relationship between wind and various wave scales has attracted significant research attention. Numerous studies have demonstrated the direct correlation between different wind-wave parameters and sea drag (Donelan, 1982; Belcher, 1998; Sullivan & McWilliams, 2010). These parameters, categorized based on wave geometry such as wave height, length, local slope, and surface curvature, or wave speed, classified by wave age or wind-sea Reynolds number, play pivotal roles in modulating sea surface drag (Dobson *et al.*, 1994; Janssen, 1997; Johnson *et al.*, 1998).

Empirical relations have been proposed in several studies, aiming to correlate the sea surface drag coefficient with wind-wave parameters (e.g., Garratt, 1977; Large & Pond, 1981; Holthuijsen, 2010). However, these studies have highlighted the complex and non-linear nature of the sea surface drag coefficient's relationship with multiple wind-wave parameters simultaneously. Review by Bryant & Akbar (2016) has underscored the challenges arising from the intricate connections among different wind-wave parameters, leading to wide scatter and inconsistencies in proposed sea surface drag coefficient relations spanning several decades.

To address these challenges, studies have begun to explore the influence of local wave properties, such as local wave slope, on shear stress, turbulence levels, and consequently, sea drag (e.g. Veron *et al.*, 2007; Buckley & Veron, 2017; Hung & Tsai, 2009; Porchetta *et al.*, 2022; Matsuda *et al.*, 2023; Yousefi *et al.*, 2024). Notably, particle image velocimetry (PIV) measurements conducted on the air side over waves by Buckley & Veron (2017) and Yousefi *et al.* (2024) have revealed that Reynolds stresses exhibit phase-locked behaviour with the wave slope. At the windward side of the waves (i.e., positive slope), flow acceleration approaching its maximum near the crest of the wave leads to significant viscous stress. Just past the wave crest, the shear layer detaches from the water surface, resulting in a dramatic drop in near-surface streamwise velocity due to flow reversal. Simulations by Hung & Tsai (2009) suggested that local wave slope and curvature could indicate the formation of small waves (capillary wave scales), which directly influence the contribution of viscous and pressure drag from waves, a finding later confirmed by Matsuda *et al.* (2023). Despite the insights gained from previous studies regarding drag distribution and turbulence on wave surfaces, the exact contribution of local slope, particularly its effect on turbulence (i.e. Reynolds stresses), remains unclear.

In this study, we conducted experimental investigations on airflow above wind-generated waves, focusing on the dependence of Reynolds stresses on wave slope, specifically the windward and leeward faces of the waves. We performed a high resolution streamwise/vertical PIV experiment spanning across the boundary layer with a wind speed of 8.4 m/s. Our PIV configuration was designed to accurately resolve turbulent motions and flow separation events, albeit within a narrow streamwise region.

MEASUREMENT FACILITY AND PROCEDURE

The experiments are conducted at the Sea Ice Wind Wave Interaction facility located in the Michell Hydrodynamics Laboratory at the University of Melbourne. The dimensions of the wave flume are 14 m in length, 0.75 m in width and 0.7 m in height, in the streamwise (x), spanwise (y) and wall-normal (z) directions, respectively. The flume is filled with water to a depth of 0.3 m, leaving a wind-tunnel test section (referred to as the air side) of 0.4 m in height extending up to the ceiling. Full details about the facility are provided in Abu Rowin *et al.* (In-press). The wind waves are generated over a fetch distance of 3.5 m, with a free-stream velocity of $U_\infty = 8.4$ m s^{-1}. At this velocity, the dominant wave properties are wave height $\eta_0 \approx 20$ mm and dominant wavelength $\lambda_0 \approx 165$ mm (Bhirawa *et al.*, 2018). In this study, the symbols u and w represent the instantaneous velocities in the streamwise and wall-normal directions, respectively. The uppercase velocity parameters (U and W) denote time-averaged velocities, while the superscript prime (u' and w') indicates parameters related to velocity fluctuations, and the angle brackets '$\langle . \rangle$' indicates averaging in the x-direction and time e.g. $\langle u'w' \rangle$.

To explore the turbulent boundary layer near and away from waves, we conducted a planar PIV experiment configured in a streamwise/wall-normal arrangement with a resolution of approximately ~ 40 µm pix^{-1}. This PIV system was designed to capture detailed turbulent motions and separation events within a limited streamwise extent. The experimental setup involved two cameras, denoted as C_1 and C_2, arranged in a stacked configuration to create a vertical field-of-view (FOV) measuring 50×150 mm in the $x \times z$ directions, as shown in Figure 1. The boundary layer thickness at the current wind speed was estimated at $\delta = 113$ mm, determined as the height where the mean streamwise velocity recovers to 99% of the freestream velocity ($0.99U_\infty$). To enhance resolution near the

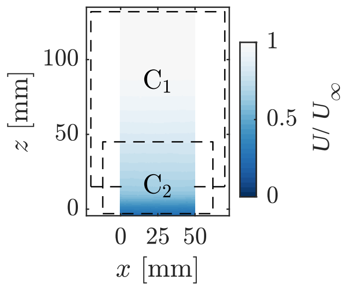

Figure 1. The resulting domains from stitching the two cameras domains showing the normalised streamwise time-averaged velocity field U by $U_\infty = 8.4$ m s^{-1}. Dashed rectangles show the domains captured by the individual cameras (C_1 and C_2).

surface, the lower camera, C_2, was independently evaluated using an interrogation window of 16×16 pixels^2. The detection of the wave surface in the PIV particle images was facilitated by an algorithm outlined in Abu Rowin *et al.* (In-press).

TURBULENCE ACTIVITY OVER WAVES

In this section, we discuss the significant turbulence observed in the flow over waves and its relation with the slope, specifically the windward and leeward faces of the waves. To illustrate this relationship, we present the Reynolds-shear stress $u'w'$ normalised by the square of the freestream velocity U_∞^2 for a selection of realisations in Figure 2. In the realisations shown in Figure 2(*a*-*c*), representing the windward faces of the waves with positive wave surface slopes, only subtle variations in $u'w'/U_\infty^2$ are evident, despite the anticipated presence of significant vertical components in this region (Buckley & Veron, 2017). Conversely, in Figure 2(*d*-*f*), characterised by recirculation on the leeward side of the wave, $u'w'/U_\infty^2$ exhibits notable variability with alternating regions of positive and negative values. Such flow patterns on the windward and leeward faces of the waves bear resemblance to those observed in the context of flow over hills (Hunt & Snyder, 1980). However, it is expected that flow separation events over waves, which result in high fluctuation signals about the time-averaged mean, are expected to differ compared with fixed-shaped topography owing to the irregularity of the wave scales and shapes.

These observations underscore the prominence of turbulence on the leeward faces of the waves compared to their windward counterparts. To show the wall-normal extent of this shear layer, Figure 3(*a*) shows the streamwise instantaneous velocity u for a chosen realisation at the leeward slope of a wave. The darkest contours near the wave surface denote reverse-flow regions ($u < 0$), attributed to strong local adverse pressure gradients akin to the flow downstream of a backward-facing step (Simpson, 1989). This reverse-flow region is more discernible in the processed view from the high-magnification camera in Figure 3(*b*), where fine-scale turbulence activity is distinctly observed on the leeward side of the wave. Here, instances of reverse velocity, accounting for less than 10% of U_∞, are evident and may exhibit higher magnitudes during more intense separation events. The instantaneous velocity profile at $x = 17$ mm in Figure 3(*b*) illustrates a sharp velocity discontinuity across the separating interface. This abrupt change was previously visualised by Kawai (1981) using smoke streaks and is also apparent in the dataset of Buckley & Veron (2017) which is an indication of a strong

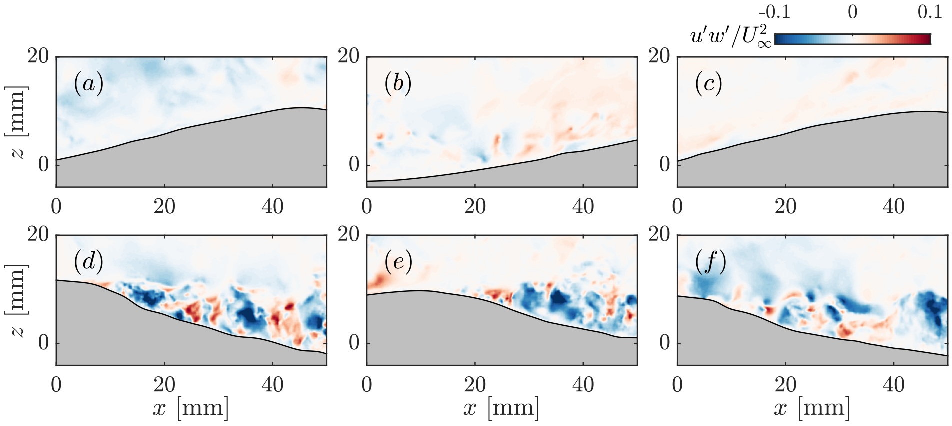

Figure 2. Reynolds-shear stress $u'w'$, normalised by the square of the freestream velocity U_∞^2, for realisations on the windward (a, b, c) and leeward (d, e, f) faces of the waves. The detected water surface is overlaid on each plot for the corresponding cases. The origin $z = 0$ is at the stationary water surface level. The flow for all the plots is from left to right.

separating shear layer. Note that the shear layer thickness in this particular instance, the height of the velocity jump, is approximately 4 mm. To better visualise the edge of the separating shear layer, we plot in Figure 3(c) the instantaneous Reynolds-shear stress ($u'w'$) for the same realisation shown in Figure 3(b).

The strong vorticity field which is typically associated with the separating shear layer can be visualised by observing the departure of the spanwise vorticity ω_y line from the wave surface as shown in Figure 3(d). Previous studies (Veron *et al.*, 2007; Reul *et al.*, 2008; Buckley & Veron, 2016) have demonstrated that the shear layer tends to be nearly horizontal as it separates from the wave, with a strong vorticity field occupying the separation region. To show the vortical activities responsible for vertical momentum transfer, swirling strength values λ_y are plotted in Figure 3(e). Swirl strength is defined as the imaginary part of the complex eigenvalue of the 2D velocity gradient tensor, as described by Adrian *et al.* (2000). Since the swirl does not carry sign information, its direction follows the sign of vorticity. Compact regions of swirl provide a means to highlight the vortex core piercing the measurement plane. Figure 3(f) depicts the eddies shed during the initial separation event along the high-shear region. These eddies are identified at the centroid of the swirling-strength region, and local Galilean decomposition is employed to illustrate individual rotating motion (i.e. by subtracting the velocity at the vortex centre for each eddy). These small eddies, as described by Jeffreys (1925), occupy the boundary between the large circulation and the main current downwind of the wave crests. The forward velocity u at the centre of these 12 depicted vortices, crudely indicating their convecting speed, varies between 7 to 46% of U_∞, significantly faster than the wave celerity. These separation-induced vortices are expected to influence the overall surface drag and further enhance gas and heat transfer across the air-sea interface (Melville, 1996). From the observation, we can conclude that turbulence imposed on the leeward side of the waves has a much larger contribution than that imposed on the windward side. This difference in contribution at each side of the wave might only extend up to the edge of the separating shear layer. All these observations derived from this section are from an instantaneous sense and the average contribution of each side of the wave (or slope) on the imposed turbulence is not clear. Thus in the following section conditional averaging analysis is applied to identify the relation of the wave slope and the turbulence at various wall-normal heights.

REYNOLDS STRESSES DEPENDENCY ON THE WAVE SLOPE

In the previous section, we demonstrated that turbulence stresses are more pronounced on the leeward side of the waves (i.e., the negative slope) mainly due to the presence of airflow separation. In this section, we further illustrate this by conditionally averaging the Reynolds stresses based on the instantaneous water surface slope $s = \partial\eta/\partial x$. It is worth noting that when defining this gradient, we initially smooth the instantaneous surface profile to retain only the large-scale undulation. To illustrate the conditional averaging procedure, we first extract the high-resolution velocity data at $z = 5.5$ mm (approximately at the peak of $\overline{u'^2}$) and plot the joint probability density function (pdf) between the wave slope s and the streamwise Reynolds stress u'^2 value as shown in Figure 4(a). It is evident that the majority of the data points are clustered around lower surface slopes (dark contour), corresponding to low u'^2 values. However, notably, the larger u'^2 values tend to occur at negative slopes $s \lesssim 0$, indicating the lee face of the wave. At this elevation, $s \approx -0.3$ yields the highest fluctuation magnitude. To assess the overall contribution of each slope to the streamwise Reynolds stress $\overline{u'^2}$, we integrate the joint pdf shown in Figure 4(a) as

$$\begin{aligned}
\int P\left(u'^2, s\right) u'^2 \,\mathrm{d}\left(u'^2\right) &= \int P\left(u'^2|_s\right) P(s)\, u'^2 \,\mathrm{d}\left(u'^2\right), && (1)\\
&= P(s) \int P\left(u'^2|_s\right) u'^2 \,\mathrm{d}\left(u'^2\right), && (2)\\
&= P(s)\, \overline{u'^2}|_s, && (3)
\end{aligned}$$

here, P represents the local probability of each variable (such as $u'^2|_s$ or s), with the subscript 's' denoting conditional averaging based on the slope of the wave. Figure 4(b) illustrates $P(s)\overline{u'^2}|_s$ as a function of s in solid black line. Note that the area under this function $\int P(s)\overline{u'^2}|_s ds = u'^2$ is the averaged stress. It is evident from this figure that Reynolds stresses detected on the lee side of the wave ($s \lesssim 0$) are responsible for almost twice the stresses observed on the wind-

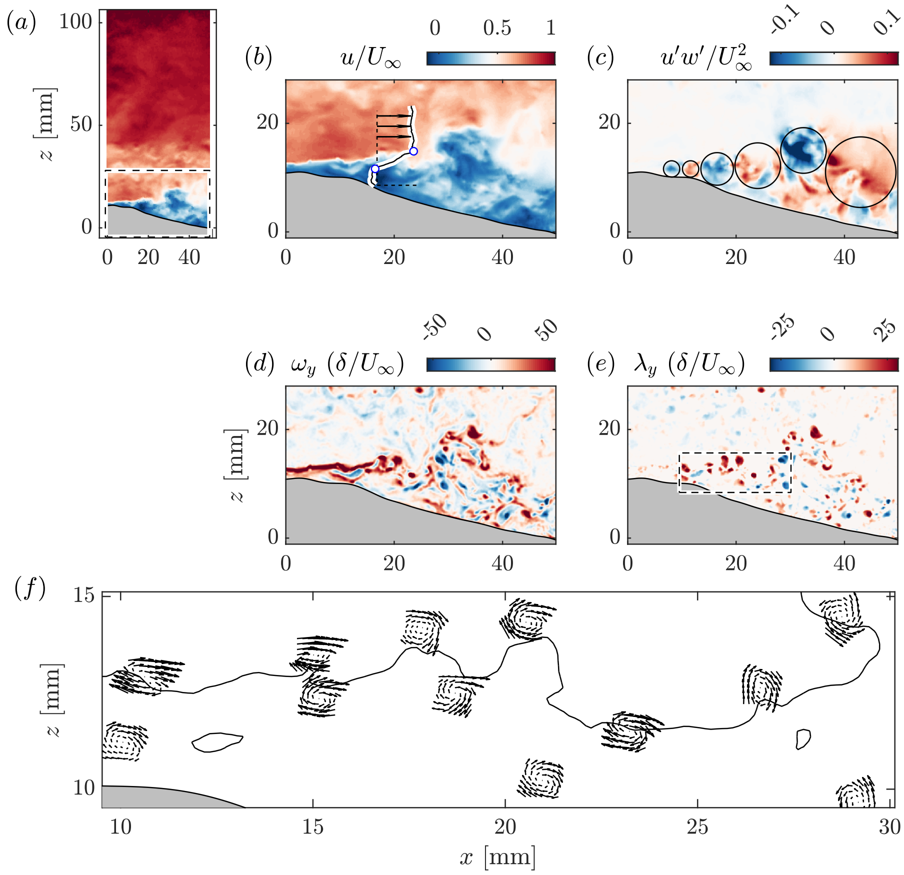

Figure 3. Example of an instantaneous velocity realisation obtained from high-resolution measurements for $U_\infty = 8.5$ m/s. (a,b) Depiction of the streamwise velocity from the stitched view of the both cameras and the higher resolution velocity field of separately processing the bottom camera. The dashed box outlines (a) outlines the FOV of the higher resolution camera (C2). The instantaneous velocity profile at $x = 17$ mm is overlaid in (b). (c) Presentation of Reynolds-shear events, with circles indicating the repeating $u'w'$ pattern. (d,e) Representation of vorticity and swirling strength fields. (f) Localised Galilean decomposition of vortices, identified by the swirl strength events. Line denotes the contour of $u = 0.3U_\infty$.

ward side. To further demonstrate the dependency of u'^2 on s, we also plot in Figure 4(b) that the probability assuming that u'^2 and s are independent $\big($i.e. $P(u'^2,s) = P(u'^2).P(s)\big)$, denoted as $P(s)u'^2$, depicted with a grey solid line. The values of $P(s)\overline{u'^2}|_s > P(s)u'^2$ at $s \lesssim -0.1$ indicate that greater u'^2 occurs on the leeward side of the wave, suggesting a dependency between wave slope and Reynolds stresses. Figures 4$(c-e)$ show the Reynolds stresses at $U_\infty = 8.4$ m s^{-1}, comparing the contributions from the wave slope of $s < -0.05$ (dashed lines) and $s > -0.05$ (dotted lines). Here the selection of $s = \pm 0.05$ is to avoid any uncertainty due to the overlap of the data points near the crest of the waves ($s = 0$). It is evident that the negative surface gradient, representing the lee side of the waves, largely contributes to the high peaks of Reynolds stress below the crest. The dashed and dotted profiles contribute to 23% and 58% of the overall Reynolds stresses, respectively. These contribution percentages may slightly vary with the expansion/reduction of the hashed region (i.e. changing the selected value of $s = -0.05$) shown in Figure 4(b). It is also illustrated in Figure 4(c) that the 'inner peak' in the Reynolds stress profiles manifests above the lee side of the wave.

It is clear from Figures 4$(c-e)$ that the turbulence variation between positive and negative wave slopes diminishes above the wave crest (shown with short vertical line), indicated by Reynolds-stress profiles collapsing for $z/\delta \gtrsim 0.13$. This phenomenon occurs despite the undulating effect of the wave extending to the very edge of the boundary layer, as shown from the time averaged velocity contour in e.g. Buckley & Veron (2016) and Abu Rowin *et al.* (In-press). Such observations imply that the 'wave-coherent' velocity fluctuations maintain equal magnitudes on both the windward and leeward faces, at least above the crest, despite the streamwise asymmetry of the waveform itself. This observation also suggests that the separating shear layer (discussed in the previous section) is primarily confined to the vicinity of the wave crest.

CONCLUSION

Understanding the intricate relationship between ocean waves and turbulent airflow at the air-water interface is fundamental to understanding environmental processes. Through Particle Image Velocimetry (PIV) experiments conducted with high magnification, we have gained insights into the turbulent stresses occurring over waves, particularly focusing on the influence of wave slope on turbulence generations.

Our analysis reveals a significant impact of wave slope on Reynolds stress, is particularly below the wave crest. Notably, the contribution from flow over the leeward faces of the wave to Reynolds stress exceeds that of the windward face by approximately twofold. The different contributions of each wave face show the importance of considering wave slope when studying turbulence dynamics over waves. Interestingly, our

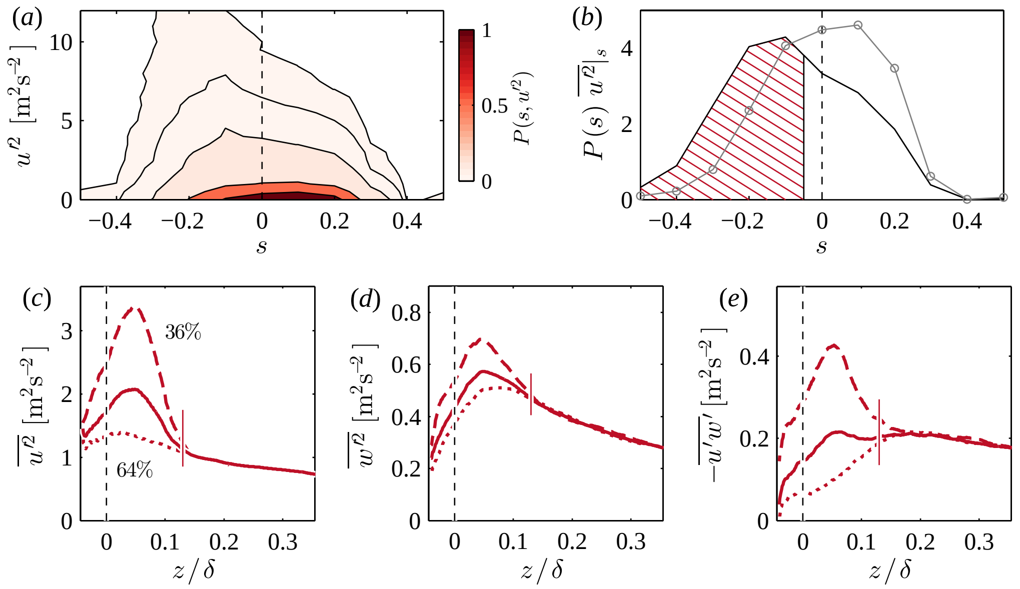

Figure 4. (a) Joint pdf between the wave slope and the streamwise Reynolds stresses $P(s,u'^2)$ at the peak location of the streamwise Reynolds stress $\overline{u'^2}$ at $z/\delta \approx 0.05$. (b) Integration of the joint pdf ($P(s)\overline{u'^2}|_s$) shown in (a) as function of s shown with the a solid black line. The grey $\circ$ symbols and line show $P(s)u'^2$ when u'^2 and s are assumed independent. Hashed region in (b) is where the data is used to plot the dashed profiles in ($c-e$). ($c-e$) time averaged streamwise u'^2 and wall-normal w'^2 Reynolds statistics and $u'w'$ Reynolds shear stresses, separated for the negative slope $s < -0.05$ (dashed lines); and positive slope $s > -0.05$ (dotted lines). The solid lines in ($c-e$) Reynolds statistics for data across the domain. The black vertical dashed lines in (a) and (b) are at $s = 0$ and in ($c-e$) are at the origin $z/\delta = 0$ at the stationary water surface level. The short vertical lines in ($c-e$) are the average location of the wave crest.

observations also indicate similarities in contributions from both sides of the wave above the crest, despite the streamwise asymmetry inherent in the wave profile. This suggests that wave-coherent velocity fluctuations maintain consistent magnitudes on both the windward and leeward faces above the crest, despite the asymmetry in the waveform.

Overall, our study highlights the significance of considering wave slope in understanding turbulence dynamics over waves and highlights the need for further research to explain the complex interplay between ocean waves and turbulent airflow in the vicinity of the wave surfaces.

REFERENCES

Abu Rowin, W., Kevin, Bhirawa, T., Lee, W. J., Philip, J., Marusic, I. & Monty, J. In-press High-resolution PIV measurement over wind-generated waves. *Exp. Fluids* .

Adrian, R. J., Christensen, K. T. & Liu, Z. C. 2000 Analysis and interpretation of instantaneous turbulent velocity fields. *Exp. Fluids* **29** (3), 275–290.

Belcher, S. E. 1998 Turbulent flow over hills and waves. *Annu. Rev. Fluid Mech.* **30** (1), 507–538.

Bhirawa, T., Kevin, Lee, J. H. & Monty, J. P. 2018 Time-resolved spatial measurements of gravity-capillary waves. In *21st Australasian Fluid Mechanics Conference. Perth, Australia*.

Bryant, K. M & Akbar, M. 2016 An exploration of wind stress calculation techniques in hurricane storm surge modeling. *J. mar. sci. eng.* **4** (3), 58.

Buckley, M. P. & Veron, F. 2016 Structure of the airflow above surface waves. *J. Phys. Ocean.* **46** (5), 1377–1397.

Buckley, M. P. & Veron, F. 2017 Airflow measurements at a wavy air–water interface using piv and lif. *Exp. Fluids* **58** (11), 161.

Dobson, F. W, Smith, S. D & Anderson, R. J 1994 Measuring the relationship between wind stress and sea state in the open ocean in the presence of swell. *Atmos. Ocean* **32** (1), 237–256.

Donelan, M. A. 1982 The dependence of the aerodynamic drag coefficient on wave parameters. In *Proc. First Int. Conf. on Meteorol. and Air-Sea Interaction of the Coastal Zone*, pp. 381–387. Amer. Meteor. Soc.

Garratt, J. R. 1977 Review of drag coefficients over oceans and continents. *Monthly weather review* **105** (7), 915–929.

Holthuijsen, L. H. 2010 *Waves in oceanic and coastal waters*. Cambridge university press.

Hung, Li-Ping & Tsai, Wu-Ting 2009 The formation of parasitic capillary ripples on gravity–capillary waves and the underlying vortical structures. *J. Phys. Ocean.* **39** (2), 263–289.

Hunt, J. C & Snyder, W. H 1980 Experiments on stably and neutrally stratified flow over a model three-dimensional hill. *J. Fluid Mech.* **96** (4), 671–704.

Janssen, J. A 1997 Does wind stress depend on sea-state or not?–a statistical error analysis of hexmax data. *Boundary-Layer Meteorol.* **83**, 479–503.

Jeffreys, H. 1925 On the formation of water waves by wind. *Proc. R. Soc. Lond. A* **107** (742), 189–206.

Johnson, HK, Højstrup, J, Vested, HJ & Larsen, Søren Ejling 1998 On the dependence of sea surface roughness on wind waves. *J. Phys. Ocean.* **28** (9), 1702–1716.

Kawai, S. 1981 Visualization of airflow separation over wind-wave crests under moderate wind. *Boundary-Layer Meteorol.* **21** (1), 93–104.

Large, W. G. & Pond, S. 1981 Open ocean momentum flux measurements in moderate to strong winds. *J. Phys. Ocean.* **11** (3), 324–336.

Matsuda, K., Komori, S., Takagaki, N. & Onishi, R. 2023 Effects of surface tension reduction on wind-wave growth and air–water scalar transfer. *J. Fluid Mech.* **960**, A22.

Melville, W. K. 1996 The role of surface-wave breaking in air-sea interaction. *Annu. Rev. Fluid Mech.* **28**, 279–321.

Porchetta, S., Carlesi, T., Rosaria, M. Vetrano, van Beeck, J. & Laboureur, D. 2022 Experimental investigation of the air-flow structure above mechanically generated regular waves for both aligned and opposed wind–wave directions. *Exp. Therm. Fluid Sci.* **133**, 110578.

Reul, N., Branger, H. & Giovanangeli, J.-P. 2008 Air flow structure over short-gravity breaking water waves. *Boundary-Layer Meteorol.* **126** (3), 477–505.

Simpson, R. L. 1989 Turbulent boundary layer separation. *Annu. Rev. Fluid Mech.* **21** (1), 205–232.

Sullivan, P. P. & McWilliams, J. C. 2010 Dynamics of winds and currents coupled to surface waves. *Annu. Rev. Fluid Mech.* **42**, 19–42.

Veron, F., Saxena, G. & Misra, S. K. 2007 Measurements of the viscous tangential stress in the airflow above wind waves. *Geo. Res. Lett.* **34** (19).

Yousefi, Kianoosh, Hora, Gurpreet Singh, Yang, Hongshuo, Veron, Fabrice & Giometto, Marco G 2024 A machine learning model for reconstructing skin-friction drag over ocean surface waves. *J. Fluid Mech.* **983**, A9.